Received May 17, 2021, accepted May 31, 2021, date of publication June 7, 2021, date of current version June 17, 2021.

Digital Object Identifier 10.1109/ACCESS.2021.3087012

Microwave Characterization of Conductive PLA and Its Application to a 12 to 18 GHz 3-D Printed Rotary Vane Attenuator

ENRIQUE MÁRQUEZ-SEGURA[1,2], (Senior Member, IEEE), SANG-HEE SHIN[2], (Graduate Student Member, IEEE), ATTIQUE DAWOOD[2], NICK M. RIDLER[3], (Fellow, IEEE), AND STEPAN LUCYSZYN[2], (Fellow, IEEE)

[1]Departamento de Ingeniería de Comunicaciones, E.T.S. Ingeniería de Telecomunicación, Universidad de Málaga, 29010 Málaga, Spain
[2]Department of Electrical and Electronic Engineering, Imperial College London, London SW7 2AZ, U.K.
[3]Department of Electromagnetic and Electrochemical Technologies, National Physical Laboratory (NPL), Teddington TW11 0LW, U.K.

Corresponding author: Stepan Lucyszyn (s.lucyszyn@imperial.ac.uk)

This work was supported in part by the Spanish Government (Agencia Estatal de Investigación, Fondo Europeo de Desarrollo Regional, Unión Europea) (AEI/FEDER, UE) under Grant TEC2016-76070- C3-3-R (ADDMATE) and Project Salvador de Madariaga under Grant PRX19/00074, and in part by the U.K. Space Agency's Centre for Earth Observation Instrumentation (CEOI) under Grant RP10G0435A202.

ABSTRACT This paper demonstrates an ultra-light weight microwave rotary vane attenuator (RVA) manufactured using polymer-based 3-D printing. In addition, for the first time, conductive polylactic acid (PLA) is rigorously characterized across both X- and Ku-bands (8 to 18 GHz); while acrylonitrile butadiene-styrene (ABS) has similarly been characterized across Ku-band (12 to 18 GHz). Using the results from the conductive PLA characterization process, an electromagnetic model was created for predicting the performance of the RVA. It is shown that, even with its complex internal geometrical features, a mix of both dielectric and conductive PLA building materials, an assembly of multiple parts and a mechanically rotating central section, our experimental proof-of-concept prototype RVA exhibits excellent measured performance across Ku-band. This tunable microwave control device represents a higher-level of functionality for additive manufacturing, when compared to a fixed (i.e., non-movable) 3-D printed structure, opening the way for other groups to routinely 3-D print custom microwave components and subsystems in the not too distant future.

INDEX TERMS Rotary vane attenuator (RVA), additive manufacturing, 3-D printing, fused deposition modelling (FDM), polymer-jetting (PolyJet), acrylonitrile butadiene-styrene (ABS), polylactic acid (PLA), conductive PLA, microwave, dielectric characterization, circular waveguide, rectangular waveguide.

I. INTRODUCTION

Rotary vane attenuators (RVAs) are used in waveguide subsystems, where precision attenuation standards and broadband (frequency invariant) operation are required. At its center is a rotating circular waveguide section, usually fed at both ends by a pair of impedance-matched TE_{10} mode rectangular-to-circular TE_{11} mode waveguide transitions. All three waveguide sections are fitted with resistive vanes, to suppress unwanted modes, ensuring close agreement to the ideal law for its attenuation, $A\,(\mathrm{dB}) = 10log_{10}\{\sec^4(\theta)\}$, where θ is the rotational angular offset of the center section's vane; providing both high accuracy and precision when direct-reading of attenuation is required [1]–[5].

Additive manufacturing using polymer-based 3-D printing is an emerging technology that is finding its way from academic research to commercial exploitation. This enabling technology has already proven itself with metal-pipe rectangular waveguides (MPRWGs) and associated components. For example, the authors have already demonstrated waveguides using various polymer-based 3-D printing technologies: fused deposition modelling (FDM) at X-band (8 to 12 GHz) [6], [7]; polymer-jetting (PolyJet) at Ku-band (12 to 18 GHz) [8]–[10]; stereolithographic apparatus (SLA) at W-band (75 to 110 GHz) [6]; PolyJet in the WM-570 band (325 to 500 GHz) [11]; and RECILS in the WM-380

The associate editor coordinating the review of this manuscript and approving it for publication was Abhishek K. Jha.

band (500 to 750 GHz) and WM-250 band (750 GHz to 1.1 THz) [12]. More recently, the authors have also demonstrated the use of FDM, SLA and ultra-low cost masked stereolithographic apparatus (MSLA) in polymer-based 3-D printed G-band (140 to 220 GHz) quasi-optical components and integrated subsystems [13].

There are very few examples of 3-D printed variable control devices reported in the open literature. The authors have previously demonstrated MPRWG: (i) variable phase shifters at both X-band [7] and Ku-band [8], based on moving acrylonitrile butadiene-styrene (ABS) dielectric inserts; and (ii) I-Q vector modulator at WM-570 band, based on laser illuminated silicon implants [11]. In addition, the preliminary results for a Ku-band RVA was reported by the authors (in a short national symposium paper, written in Spanish) [9], based on moving conductive polylactic acid (PLA) resistive vanes.

Indeed, conductive PLA has added new functionality to polymer-based 3-D printing of microwave components. For example, in 2018, Chan *et al*. implemented conductive PLA flanges, for sealing Ku-band waveguides with liquid metal filled walls, as a low-cost solution to avoid conventional metallic plating of 3-D printed parts [14]. This work employed Conductive Graphene PLA (Black Magic 3D, USA) having a volume resistivity at DC of only 0.6 Ω**.**cm. Having a higher volume resistivity at DC, in addition to our Ku-band RVA vanes [9], the authors have demonstrated the use of Proto-pasta conductive PLA to make G-band tessellating pyramidal-array radiation absorbent material (RAM) for quasi-optical subsystems [13].

Here, details of the proof-of-concept 3-D printed rotary vane attenuator are given for the first time, while also rigorously characterizing Proto-pasta conductive PLA in both X- and Ku-bands; validating this process by characterizing ABS at Ku-band.

II. RVA DESIGN

A. PRINCIPLE OF OPERATION

Figure 1(a) illustrates an exploded-view for a basic three-section circular waveguide RVA, with corresponding orthogonal electric (E)-field decomposition at the different reference planes shown in Fig. 1(b) [4], [15]. Each section initially has an E-field absorbing septum (resistive vane) in the horizontal plane, which attenuates any parallel E-field component. Only the normal E-field component can propagate through the waveguide sections [5]. Therefore, if the central section is not rotated from its horizontal plane (i.e., $\theta = 0$), there is ideally no attenuation; no current is induced in the absorbing septum. Conversely, with $\theta = 90°$, attenuation is theoretically infinite [16]; with commercial RVAs limited to 60-70 dB of attenuation in practice.

An important feature of the RVA is that insertion phase and, therefore, differential-phase group delay do not change as the rotational angular offset varies within its operational range of $0 \leq \theta \leq 90°$ [3]. Moreover, the return loss performance

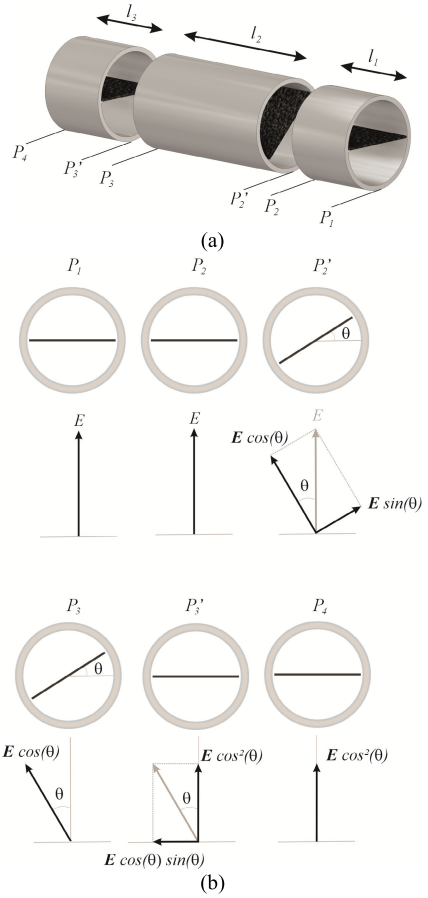

FIGURE 1. Basic three-section circular waveguide rotary vane attenuator principle of operation: (a) exploded-view with resistive vanes (shown in black); and (b) orthogonal E-field decomposition at different reference planes [4], [15].

should not degrade across this operational range. For this reason, the vane should not be highly conductive. To this end, Proto-pasta conductive PLA is an excellent choice for a 3-D printed RVA, as it acts as an electromagnetic absorber.

With rectangular waveguide test ports, it is necessary to introduce TE_{10} mode rectangular-to-circular TE_{11} mode waveguide mode-matching transitions, as illustrated by the computer-aided design (CAD) renderings shown in Fig. 2.

Figure 3 shows the CAD renderings for our Ku-band RVA design, complete with variable attenuation control screw, bi-directional clamps and support stand. Figures 3(b) to 3(d) illustrate the bi-directional clamps, designed to connect the different waveguide sections of the RVA together; allowing movement with the same half-clamp orientation. To characterize the back-to-back transitions, movement is avoided with the opposite half-clamp orientation.

To calibrate the angle of rotation over its 90° range, the center section has an integrated 3-D printed helical gear, mechanically coupled to an endless screw that is attached to the support stand, as illustrated in Fig. 3(a). In addition, 3-D printed alignment peaks and troughs, at angular intervals of 6°, allows an estimate of the expected level of attenuation.

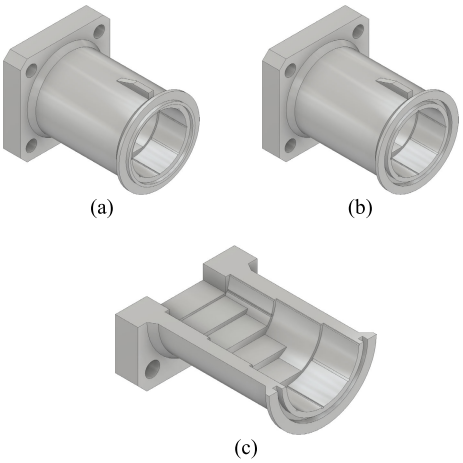

FIGURE 2. CAD renderings of the rectangular-to-circular waveguide transition (resistive vanes not shown): (a) male circular interface; (b) female circular interface; and (c) cross-sectional view of the female circular interface transition.

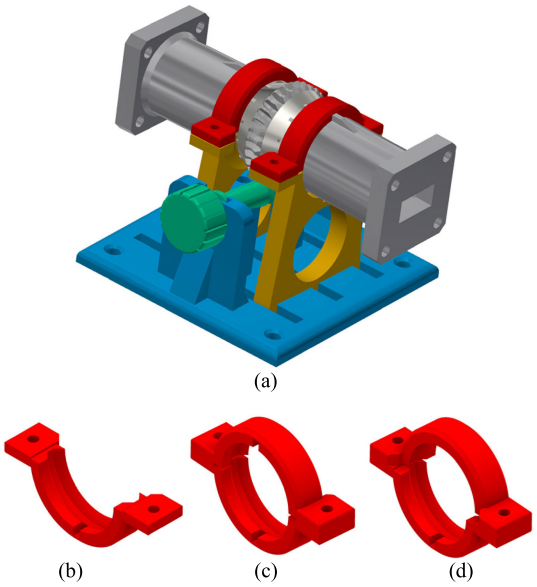

FIGURE 3. CAD renderings for the all 3-D printed rotary vane attenuator: (a) complete RVA assembly with integrated variable attenuation control screw (shown in green), bi-directional clamps (shown in red) and support stand (shown in blue); (b) one half-clamp; (c) two half-clamps in the same orientation to allow rotation; and (d) two half-clamps in the opposite configuration to avoid rotation.

B. WAVEGUIDE TRANSITIONS

At the measurement ports, the rectangular waveguide flanges are based on WR-62 standards, operating at Ku-band, having internal cross-sectional dimensions of $a = 15.7988$ mm and $b = 7.8994$ mm. This band is suitable for PolyJet 3-D printing, as issues associated with 3-D print accuracy and surface roughness are negligibly small for most applications [8]–[10]; the latter may be improved with metallization.

Our circular waveguide is based on WC-80 standards; having a diameter commensurate with the widest dimension of the WR-62 rectangular waveguide. For the circular waveguide, the lower-order cut-off frequencies f_c for the transverse electric (TE) and transverse magnetic (TM) modes are: $f_c^{TE_{11}} = 1.84118 f_{co} = 8.679$ GHz; $f_c^{TM_{01}} = 2.40483 f_{co} = 11.336$ GHz; $f_c^{TE_{21}} = 3.05424 f_{co} = 14.397$ GHz; and $f_c^{TE_{01},TM_{11}} = 3.83171 f_{co} = 18.062$ GHz, where $f_{co} = c/2\pi r = 4.713836$ GHz, c is the speed of light in free space and $r = 10.122$ mm is the ideal internal radius for the WC-80 circular waveguide.

While the TE_{01} and TM_{11} modes are theoretically just above the 18 GHz frequency of interest, within a lossy environment, it may be possible to *'see'* their influence at the upper end of Ku-band. Similarly, if not completely suppressed, the influence of damped TM_{01} and TE_{21} modes may be *'seen'* in Ku-band [17], [18]. These modes will cause resonances, which can be suppressed with the use of linearly-tapered resistive vanes [19], [20], as illustrated in the mated-pair (male and female) back-to-back transitions shown in Fig. 4, which also illustrates our quarter-wavelength stepped-impedance tapers. Note that all three waveguide sections incorporate linear slotting groves, to accurately position and support the resistive vanes. As can be seen in Fig. 4(b), the simulated E-field slices show excellent mode conversion from the input rectangular TE_{10} mode to circular TE_{11} mode to output rectangular TE_{10} mode.

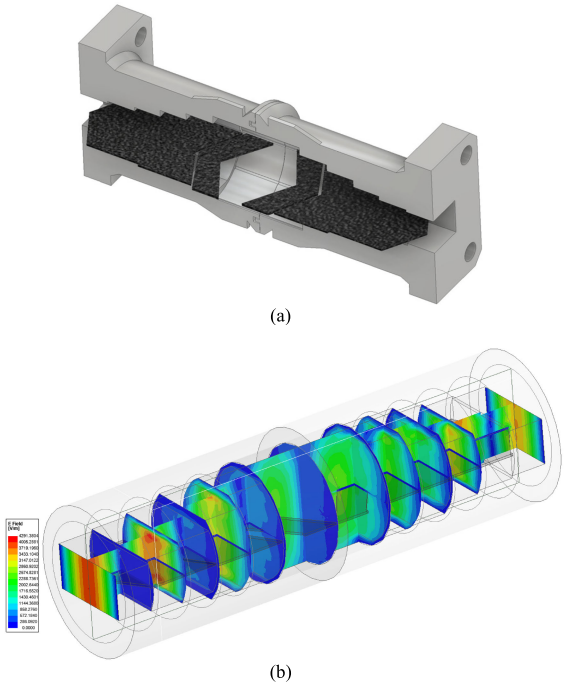

FIGURE 4. Simulation of the mated-pair (male and female) back-to-back rectangular-to-circular waveguide transitions, representing a solid silver outer structure (shown in light grey): (a) CAD rendering with higher-order mode-suppressing linear-tapered resistive vanes (conductive PLA, shown in black); and (b) E-field simulation plot at 15 GHz.

C. ROTARY VANE ATTENUATOR

Figure 5 illustrates the main three-section waveguide assembly of the rotary vane attenuator. The central section has a

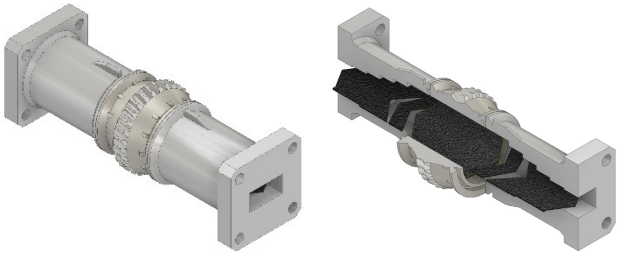

FIGURE 5. CAD renderings for the three-section waveguide assembly of the rotary vane attenuator, representing a solid silver outer structure (shown in light grey): (a) complete assembly; and (b) cross-section showing absorbers (conductive PLA, shown in black) in the fixed transitions and the rotating center section.

male circular interface on one side and female on the other; making it compatible with the two transitions.

As can be seen in Fig. 6, for different values of rotational angular offsets, the simulated E-fields maintain excellent mode conversion from the input rectangular TE_{10} mode to circular TE_{11} mode to output rectangular TE_{10} mode. As would be expected, as θ increases, the E-field strength does not change within the input transition; decaying within the central and output transition sections.

III. ADDITIVE MANUFACTURING AND METALIZATION

A. 3-D PRINTING

Different additive manufacturing (3-D printing in this case) technologies are employed in our RVA implementation. At the University of Malaga, a PolyJet 3-D printer (Stratasys Objet260 Connex3 [21]) is used for fabricating the waveguide parts. This printer has a *z-axis* build resolution that equates to a minimum layer height of 16 μm, with *x-* and *y-axis* build resolutions of 42 μm.

Digital ABS Plus is the polymer used for printing [22]. This material has similar mechanical properties as conventional ABS, but printed by jetting drops of photopolymer resin onto the build plate. It is cured using ultraviolet light after each layer is deposited. Digital ABS Plus exhibits high impact strength with high-temperature resistance and heat deflection temperature up to 95°C. This material also offers a polymerized density of only 1.18 g/cm^3 [23] (c.f., brass, having a density of 8.73 g/cm^3, traditionally used in the fabrication of waveguides at microwave frequencies).

As will be fully discussed in Section IV, the resistive vanes are realized using Proto-pasta conductive PLA, which is FDM 3-D printed (using a Raise3D Pro 2 printer) at Imperial College London.

Finally, all other mechanical parts (i.e., screw, bi-directional clamps and support stand) are made by FDM 3-D printing (using an Ultimaker 3 printer) of conventional ABS, having a minimum layer thicknesses of approximately 60 μm.

B. METALIZATION

The polymer-based waveguide parts are fully metallized, using the commercial Jet Metal^{TM} silver spray process, which is reported to have a thickness dependent volume resistivity that matches pure bulk silver of 1.59 $\mu\Omega$.cm, with 2.5 to 3 μm thick layers [23]. This process is based on a sequential supply of silver ions (Ag+) and a reducing agent, using a double nozzle paint spraying gun. The thickness of the silver layer is controlled by monitoring the time allowed for the reaction, as this is a well understood process, dependent on a specific ambient temperature and pressure [23].

Here, the Digital ABS Plus parts are metallized with a 2 μm thick layer of silver, which is over three times the skin depth δ at the lowest frequency of operation (i.e., $\delta(12\ \text{GHz}) \sim 0.6\ \mu m$).

IV. MATERIAL CHARACTERIZATION

Characterization of 3-D printed building materials is of particular interest at both X- and Ku-bands, because high performance passive waveguide components (even those having complex structures) can be easily manufactured at these frequencies. For example, Shin *et al.* recently demonstrated a fully integrated polymer-based 3-D printed Ku-band steerable phased-array antenna subsystem, consisting of 26 waveguide circuit elements (1 × flange, 6 × mitred bends, 3 × power splitters, 4 × tunable delay lines, 4 × 90° twists, 4 × bent interconnects and 4 × H-plane sectoral horn antennas) [8].

Using two simple characterization approaches, Huber *et al.* [24] reported results from 2 to 10 GHz for 3-D printed Proto-pasta conductive PLA. This filament is made by ProtoPlant Inc. (USA), for FDM 3-D printing; the polymer composite is made with Natureworks 4043D PLA, a dispersant and 20% conductive carbon black powder [25].

Using 1 cm × 1 cm × 1 cm cubic samples, ProtoPlant measured its DC resistance by simply clamping two full sheet conductors on opposite surfaces of the sample [25]. With molded resin (i.e., not 3-D printed), they report a volume resistivity at DC of 15 Ω**.**cm. With 3-D printed samples, they reported effective volume resistivities at DC ρ_o of 30 Ω**.**cm along layers (*x-y* plane of the build surface) and 115 Ω**.**cm against layers (build *z*-direction) [25], [26]; clearly indicating anisotropic behavior at DC. With the former, from a detailed study by Flowers *et al.* with Proto-pasta conductive PLA at low frequencies, ρ_o was found to be 12 Ω**.**cm along layers [27]. With the latter, Huber *et al.* [24] re-quote the value of 115 Ω**.**cm from ProtoPlant.

The first characterization approach [24] involves a 1 inch length sample inserted into a custom 3 inch air-filled computer numerical control (CNC)-milled split-block X-band (WR-90) metal-pipe rectangular waveguide; reporting average values for complex effective relative permittivity $\tilde{\varepsilon}_{reff} = \varepsilon'_{reff} - j\varepsilon''_{reff}$. For example, the dielectric constant (ε'_{reff}) and loss tangent ($tan\delta = \varepsilon''_{reff}/\varepsilon'_{reff}$) of 6.414 and 0, respectively, were reported for their FDM 3-D printed conductive PLA sample, using a waveguide slotted-line measurement system and recording the voltage standing-wave ratio (VSWR) and phase shift with its Klystron source operating from 9 to 10 GHz [24]. The direction of propagation for the

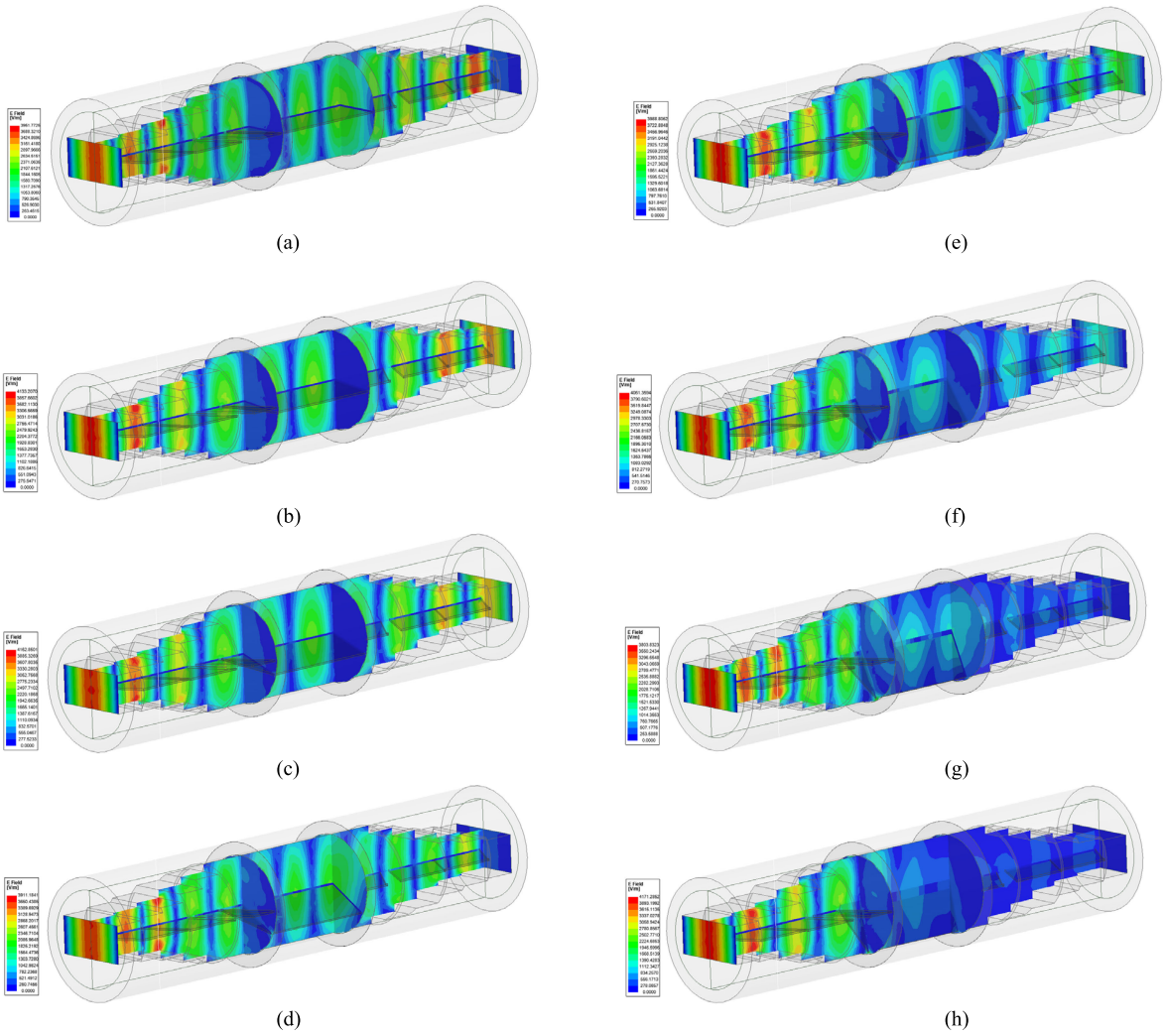

FIGURE 6. E-field simulation plots at 15 GHz for different values of rotational angular offsets: (a) $\theta = 0°$; (b) $\theta = 6°$; (c) $\theta = 18°$; (d) $\theta = 30°$; (e) $\theta = 42°$; (f) $\theta = 54°$; (g) $\theta = 66°$; (h) $\theta = 78°$.

TE_{10} mode within the dielectric-filled section of MPRWG is against layers [28].

The second characterization approach [24] employs the Keysight 85070E Dielectric Probe Kit (high-temperature configuration [29]), using one-port open-ended coaxial line measurements of their 1 cm × 1 cm × 1 cm cubic samples; with its 19 mm diameter flange, the dielectric probe is first calibrated using the default air, short and water calibration standards. Note that this kit is more suited for liquids and semi-solids, with Keysight stating the following caveats [29]: (i) *"Material is "infinite" in size, non-magnetic, isotropic (uniform orientation) and homogeneous (uniform composition)"*; (ii) *"Solids have a single, smooth, flat surface with gap-free contact at the probe face."* and *"sample must be as flat as the probe face, which is lapped to ± 100 μ inches."* (i.e., ±2.54 μm); (iii) *"Not recommended for low loss (loss tangent < 0.5) materials with $\varepsilon'_{reff} > 5$"*; and (iv) sample *"diameter > 20 mm"* and *"thickness > 20 mm/$\sqrt{|\tilde{\varepsilon}_{reff}|}$."*

Practical FDM 3-D printed samples are neither isotropic, homogeneous or capable of having truly flat surfaces [30]. Nevertheless, with the dielectric probe placed against the much smoother bottom build surface [28], Huber *et al.* found the conductive PLA sample to be frequency dispersive from 2 to 10 GHz; with ε'_{reff} decreasing and both ε''_{reff} and $tan\delta$ increasing as frequency increases, and reporting average values of $\varepsilon'_{reff} = 6.811$ and $tan\delta = 0.493$ from 9 to 10 GHz [24].

In 2017, Faenger *et al.* reported the spectroscopic results for their 3 cm × 3 cm × 1 cm Proto-pasta conductive PLA sample, between 0.25 and 7 GHz [31]. Unfortunately, no details were given on the 3-D printer used or spectroscopic techniques employed in their work. Nevertheless, as expected, ε'_{reff} decreases as frequency increases; while the loss tangent remained relatively constant with $tan\delta \approx 0.5$ across this relatively ultra-broad bandwidth.

More recently, in 2018, Kjelgard *et al.* characterized FDM 3-D printed Proto-pasta conductive PLA (which they refer to

TABLE 1. Microwave dielectric properties for Proto-pasta conductive PLA reported and †calculated to a first-order of approximation.

	ρ_o (Ω·cm)		Frequency, f (GHz)	ε'_{reff}		ε''_{reff}		$tan\delta$	
	Along	Against		Along	Against	Along	Against	Along	Against
ProtoPlant [25], [26]	30	115	3	–	–	20†	5†	–	–
			10			6†	2†		
Flowers *et al.* [27]	12	–	3			50†	–		
			10			15†			
Faenger *et al.* [31]	–	–	0.25	–	37.7	–	19.4	–	0.5
			1		29.1		11.1		0.4
			2		23.0		10.9		0.5
			3		20.0		9.8		0.5
			4		17.6		8.6		0.5
			5		16.1		7.9		0.5
			6		15.1		7.0		0.5
			7		14.1		6.0		0.4
Kjelgard *et al.* [32], [33]	–	–	2.4	–	30.0	–	46.9	–	1.6
			3		21.7		39.2		1.8
			4		16.0		30.1		1.9
Huber *et al.* [24] (First Method)	–	115 (from ProtoPlant)	9-10	–	6.414	–	0	–	0
Huber *et al.* [24] (Second Method)					6.811		3.358		0.493
This work using Combined X + Ku Band Modeling (‡Margin of Error)	–	26	7.5	10.38±0.49	12.90±0.06	10.84	13.49	1.04±0.03	1.05±0.05
			10	9.58±0.46	11.70±0.09	8.72	10.75	0.91±0.03	0.92±0.06
			12	9.11±0.49	11.00±0.49	7.59	9.31	0.83±0.07	0.85±0.08
			15	8.56±0.30	10.19±0.19	6.41	7.81	0.75±0.01	0.77±0.03
			18	8.13±0.39	9.58±0.26	5.59	6.77	0.69±0.03	0.71±0.05

‡The ± intervals indicate the margin of error due to sample reproducibility, which is the dominant source of uncertainty for these parameters. Random errors, due to lack of measurement repeatability, do not contribute significantly to this uncertainty.

as 'graphite/PLA') in the WR-284 band (2.60 to 3.95 GHz) [32], [33] and verified their results using the commercial Keysight N1500A-100 Materials Measurement Suit [34]. In their work, with target dimensions of 72.136 mm × 34.036 mm × 10 mm (in practice having slightly chamfered corners), a cuboid is 3-D printed using the Ultimaker 3 printer (with 100 μm layer thickness and 100% infill settings), having a direction of propagation for the TE_{10} mode against layers [33]. Kjelgard *et al.*, also found their conductive PLA sample to be frequency dispersive, between 2.4 to 4 GHz, with extracted values of $\varepsilon'_{reff}(2.4\text{ GHz}) = 30.0$ and $\varepsilon''_{reff}(2.4\text{ GHz}) = 46.9$ decreasing to $\varepsilon'_{reff}(4\text{ GHz}) = 16.0$ and $\varepsilon''_{reff}(4\text{ GHz}) = 30.1$; resulting in an increasing loss tangent, from $tan\delta(2.4\text{ GHz}) = 1.6$ to $tan\delta(4\text{ GHz}) = 1.9$.

It is interesting to note that, to a first-order of approximation, the imaginary part of the effective relative permittivity $\varepsilon''_{reff} \sim (\omega\varepsilon_o\rho_o)^{-1} \cong 1.80/\rho_o$ at 10 GHz, where ω is angular frequency and ε_o is the permittivity of free space; giving an order-of-magnitude prediction of $\varepsilon''_{reff}(10\text{ GHz}) \sim 2$ against layers, using the effective volume resistivity quoted by ProtoPlant [25]. This can be compared with those by Huber *et al.* [24], with extracted average ε''_{reff} values of 0 and 3.358, from 9 to 10 GHz, from their respective first and second characterization approaches. Moreover, with $\varepsilon''_{reff} \sim (\omega\varepsilon_o\rho_o)^{-1} \cong 6.00/\rho_o$ at 3 GHz, a value of $\varepsilon''_{reff}(3\text{ GHz}) \sim 5$ against layers, predicted using ProtoPlant data, can be compared with 39.2 from Kjelgard *et al.* [32].

Due to the significant opacity (i.e., optical depth) of conductive PLA, accurately characterizing this material is challenging at millimetre-wave frequencies and shorter wavelengths. Nevertheless, Hernandez-Serrano *et al.* reported the refractive index and absorption coefficient between 0.4 and 3 THz, using terahertz transmission spectroscopy; from a 220 μm thick solid disk sample, FDM-printed using a 400 μm Olson ruby nozzle (3DVerkstan AB, Sweden) [35]. With opacity values increasing from approximately 1 to 6, as frequency increases from 0.4 to 3 THz, Proto-pasta conductive PLA can be considered as semi-opaque within this particular frequency range [35].

A summary of reported results for the microwave characterization of Proto-pasta conductive PLA is shown in Table 1. It can be seen that, even though there is agreement that this FDM 3-D printed material exhibits frequency dispersive dielectric properties, the little information that is reported in the open literature is very inconsistent.

With FDM 3-D printing, just as very high loss conductive PLA has demonstrated its use as a key part for realizing a 3-D printed mechanically tunable variable attenuator [9], very low loss ABS has demonstrated its use as a key part for realizing 3-D printed mechanically tunable variable phase shifters [7], [8].

Sun and Lucyszyn recently proposed an accurate spectroscopic technique, based on free-space measurements of a dielectric sheet sample under test, using a graphical approach for material characterization [36]. This was then adapted for

rectangular waveguide measurements and further enhanced to resolve ambiguities in the $n-\kappa$ solution space for complex refractive index $\tilde{n} = n - j\kappa$ [30]; with FDM 3-D printed ABS being the dielectric under test at X-band. In this new work, FDM 3-D printed ABS is characterized at Ku-band, to act as a verification reference material, as there is no scientific reason for its dielectric constant to change significantly between X- and Ku-band frequencies. Here, the direction of propagation for the TE_{10} mode within the dielectric-filled MPRWG thru line is also against layers [30]. In addition, FDM 3-D printed Proto-pasta conductive PLA is characterized at both X- and Ku-bands and directly compared with the results at X-band from Huber *et al.* [24].

A. MEASUREMENT SET-UP

All measurements were performed by the U.K.'s National Physical Laboratory (NPL), using a vector network analyzer (VNA); with a pair of standard waveguide test ports and calibrated with either WR-90 [30] or WR-62 [8] waveguide primary reference standards. The measurement set-up employs a MPRWG thru line for each band; these are nominally air-filled quarter-wavelength sections of MPRWG operating in the dominant TE_{10} mode (normally used as a calibration standard). The cuboid samples are inserted to completely fill (ideally) the thru line; having target internal cross-section dimensions for X-band(WR-90)/Ku-band(WR-62) of: width $a = 22.860/15.7988$ mm and height $b = 10.160/7.8994$ mm. In addition, length $l = 9.626/6.676$ mm for X/Ku-bands. Note that $l = \lambda_g/4$ corresponds to a quarter-wavelength air-filled MPRWG thru line at a frequency $f_{\lambda g/4} = c/4l \cdot \sqrt{1 + (2ml/a)^2}$ for TE_{m0} modes; with our lengths, this frequency is approximately the geometric mean between the recommended waveguide band-edge frequencies. Similarly, $l = \lambda_g/2$ corresponds to a half-wavelength air-filled MPRWG thru line at a frequency $f_{\lambda g/2} = c/2l \cdot \sqrt{1 + (ml/a)^2}$ for TE_{m0} modes.

B. CUBOID SAMPLE AND VANE 3-D PRINTING

FDM 3-D printing was used to fabricate all the cuboid samples and resistive vanes; with different part types printed in separate batches, and multiple batch printing to provide redundancy. The ABS reference sample was fabricated with Formfutura's 2.85 mm filament diameter Premium ABS – White – using an Ultimaker 2 FDM 3-D printer. The Ultimaker Cura [37] slicing software was set to produce a 100 μm layer height and 100% theoretical infill density. This manufacturing setup was previously demonstrated at Ku-band [8], but only the dielectric properties extracted at X-band were used [30].

The 3-D printed Premium ABS – White – reference is believed to be chemically the same as the Premium ABS – Frosty White – used by Sun *et al.* [30] with our X-band characterization, both sourced from Formfutura B.V. (Netherlands) with a rebranding from 'Frosty White' to 'White'; this ensures material traceability. Figure 7(a) shows the standalone Ku-band sample, while Fig. 7(b) shows the same sample snuggly fitting inside the MPRWG thru line.

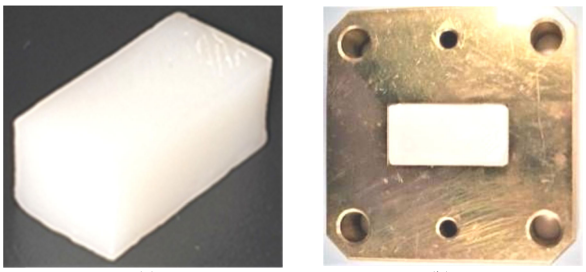

(a) (b)

FIGURE 7. Ku-band FDM 3-D printed ABS reference sample photographs for TE_{10} mode propagation against layers (in the build *z*-direction): (a) standalone, showing small defects when compared to an ideal cuboid; and (b) *in-situ* within the MPRWG thru line with TE_{10} mode propagation against layers.

In practice, scalloping (in the form of sinusoidal-like surface patterning) exists along the vertical build *z*-direction, having a spatial period of 100 μm – matching the layer height printer setting [6]. Moreover, the sub-100% infill and the straight paths of the alternating layers printed orthogonal to one another has been previously described as a 3-D woodpile structure (being non-homogeneous and porous) [30]. Therefore, dielectric anisotropy is inherently introduced from the geometric orientation of the unintended air channels; void densities are expected to be different along and against layers.

In addition, X- and Ku-band Proto-pasta conductive PLA cuboid sample pairs are manufactured, such that the direction of propagation for the dominant TE_{10} mode within the dielectric-filled MPRWG thru line is oriented both along and against layers, as illustrated in Figs. 8(a) and 8(b), respectively, in order to observe the inherent effects of dielectric anisotropy with FDM 3-D printing.

With both the cuboid samples and resistive vanes, because the 1.75 mm filament diameter Proto-pasta conductive PLA filament is more flexible (due to the addition of carbon black powder), a different FDM 3-D printer setup had to be adopted. Ultimaker 2's extrusion system has inherent lag between the extruder's feed gear and its hot-end nozzle, which causes flexible filaments to stretch and tangle within the extruder. As a result, the Raise3D Pro2 3-D printer is chosen, as it has a direct-drive extrusion system that feeds the filament directly into the hot-end nozzle. In addition, with the IdeaMaker slicing software [38], our custom print setup gives a slower print speed (50% slower than that for dielectric PLA) and higher printing temperature (30°C higher than that for dielectric PLA) to prevent nozzle blockage and abrasion. Moreover, the top surface of each 3-D printed sample is smoothed using the IdeaMaker's surface ironing function. Finally, the cuboids are lightly trimmed with high grit sandpaper, to ensure a snug fit inside the MPRWG thru line. In practice, the cuboids have X/Ku-band average spatial dimensions of $a = 22.66/15.60$ mm, $b = 10.05/7.83$ mm and $l = 9.58/6.76$ mm; errors of up to 2.3% clearly indicates non-ideal manufacturability using our low-cost FDM 3-D printer technology.

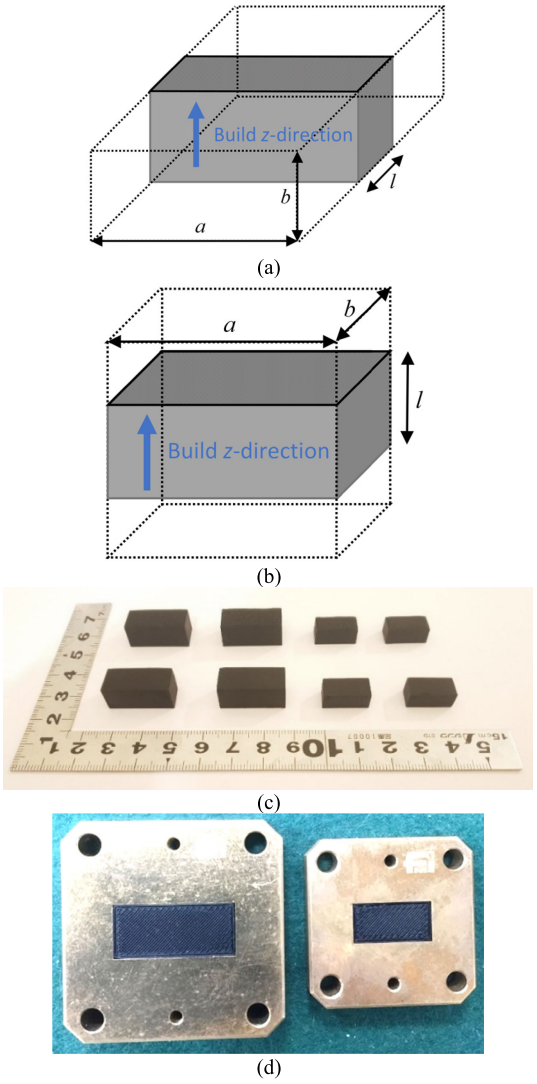

FIGURE 8. FDM 3-D printed Proto-pasta conductive PLA cuboid sample pairs: (a) orientation illustration for TE_{10} mode propagation along layers (in the *x-y* plane of the build surface); (b) orientation illustration for TE_{10} mode propagation against layers (in the build *z*-direction); (c) photograph of the X-band (left half) and Ku-band (right half) similar sample pairs. TE_{10} mode propagation along layers (top row) and against layers (bottom row). The major divisions on the ruler scales are in units of centimeters; and (d) X-band (left) and Ku-band (right) samples *in-situ* within MPRWG thru lines with TE_{10} mode propagation against layers.

The rotary vane inserts did not require further processing, as they were sufficiently thin and showed a good fit inside the circular waveguide sections. The manufactured vane is shown in Fig. 9. Here, five 100 μm thick layers are printed, giving a target vane thickness of 500 μm (c.f., commercial RVA that employ vanes having a thickness of only 100 μm); in practice this was measured to be $\sim$ 440 μm – while the average thickness for the complete set of five parts for the RVA is approximately 460 μm. The theoretical 100% infill density was also not achieved, as seen by the woodpile structure from the bottom two layers that are visible in Fig. 9(b).

In practice, the resulting infill is approximately 50% (mainly due to a reduced extrusion flow rate for the bottom

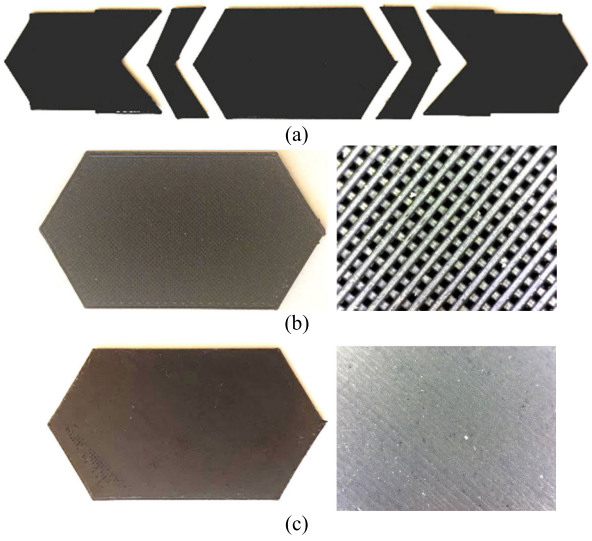

FIGURE 9. 3-D printed Proto-pasta conductive PLA resistive vanes with propagation along layers: (a) complete set of five parts for the RVA; (b) bottom surface of the rotary vane, complete view (left) and zoomed-in view (right); (c) top surface of the rotary vane, complete view (left) and zoomed-in view (right). The central piece has a vertical height of 20.3 mm and tip-to-tip width of 36.7 mm, while the printed track spacing has a period of 400 μm.

two layers), with 3-D printed track widths reduced from the ideal 400 μm setting to only $\sim$200 μm; this avoids the vanes sticking to the build plate. It can be seen in Fig. 9(c) that the top layer is ironed and so the infill density cannot be easily established.

C. KU-BAND ABS SAMPLE CHARACTERIZATION

The measured $|S_{11}|^2$ and $|S_{21}|^2$ for the ABS-filled MPRWG thru section are shown in Fig. 10(a) for Ku-band. Using the simplistic brute-force fit of $|S_{21}|^2$ (with the very accurate variational method [30]) at the Fabry-Perot resonance frequency of 15.80 GHz yields values of $\varepsilon'_{reff}(15.80\,\text{GHz}) = 2.3725$ and $tan\delta(15.80\ \text{GHz}) = 0.0014$. Alternatively, using the accurate automated renormalization spectroscopic technique [30], the extracted dielectric properties for the ABS reference sample is shown in Fig. 10(b). This technique is exactly the same as described by Sun *et al.* [30] and employs single (l-)stage, l-stage with perfect electrical conductor (PEC) reflection, cascaded ($2l$-)stage and a half ($l/2$-)stage in order to perform the extraction. The software algorithm was first run with a coarse 100 $\times$ 100 grid resolution, within the following expected bounds: $1 < \varepsilon'_{reff} < 15$ and $0 < tan\delta < 1.5$. Then, a small portion of the solution space was identified and the grid resolution was increased to 1000 $\times$ 1000.

Due to the inhomogeneity caused by FDM 3-D printing, spectral anomalies are excited at 14.25, 15.75 and 16.90 GHz, corresponding to the high Q-factor TE_{201}, TE_{011} and TE_{111} open-box mode resonances, respectively. As a result, the extracted dielectric properties in the vicinities of these frequencies should be ignored in practice [30]. As such, the dielectric constant will not exhibit

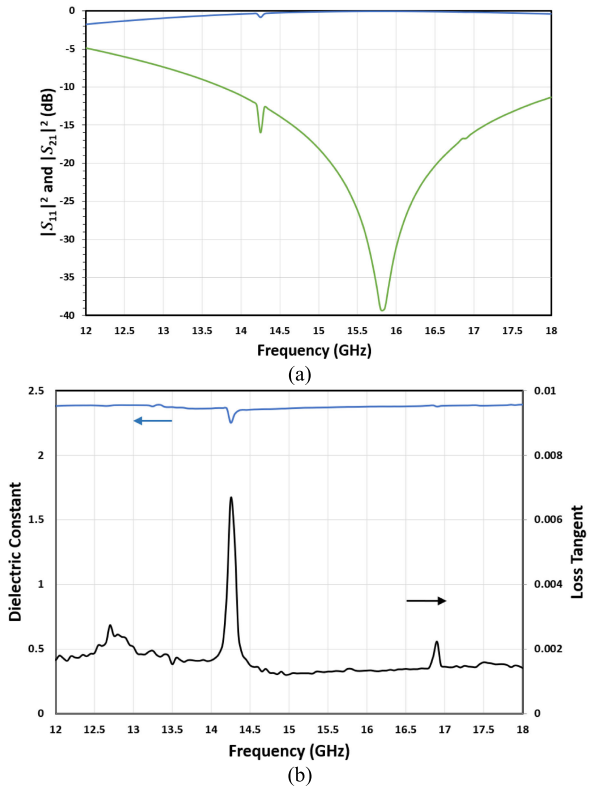

FIGURE 10. FDM 3-D printed Formfutura Premium ABS (White) reference sample characterization at Ku-band: (a) S-parameter measurements for the dielectric-filled MPRWG thru line, with $|S_{11}|^2$ in green and $|S_{21}|^2$ in blue; and (b) extracted dielectric properties, with dielectric constant ε'_{reff} in blue and loss tangent $tan\delta$ in black.

any significant frequency dispersion within Ku-band. The resulting band-average values extracted for dielectric constant and loss tangent are $\varepsilon'_{reff} = 2.36$ and $tan\delta = 0.0016$ across Ku-band; which are very close to values obtained using brute-force extraction. Moreover, the FDM 3-D printed ABS samples previously reported for X-band, have band-average extracted values of $\varepsilon'_{reff} = 2.31$ and 2.33 for two independent samples and $tan\delta = 0.0015$ for both samples; this demonstrates good agreement (<2.2% discrepancy) in the dielectric constant, between our new results at Ku-band and those previously reported at X-band [30].

The closeness of agreement within and between these bands provides excellent verification for our conductive PLA characterization process; while open-box mode resonances are strongly damped with conductive PLA samples.

Note that, in 2016, Castles *et al.* characterized 'pure ABS' across Ku-band [39]. This particular ABS is MFI-22 (Styrolution, Germany). Its raw pellets were subsequently extruded into filaments (with a number of other intermediate processing steps, which includes drying polymer sheets that are then ground using a kitchen blender into a coarse powder) and finally samples are 3-D printed using a Makerbot Replicator 2X desktop 3-D printer. Values of $\varepsilon'_{reff} = 2.57$ and $tan\delta = 0.469$ were reported for their 'pure ABS' at 14.83 GHz, using a split-post dielectric resonator method. The dielectric constant value was confirmed using 7.9 mm × 15.8 mm rectangular waveguide measurements, with a Nicholson-Ross-Weir extraction method, giving a band-average $\varepsilon'_{reff} = 2.60$ across Ku-band. There are many reasons for the differences in extracted dielectric property values, between those reported here and by Castles *et al.*, which are attributed to material processing, printing and metrology [30].

D. X-AND KU-BAND CONDUCTIVE PLA SAMPLE CHARACTERIZATION

The measured $|S_{11}|^2$ and $|S_{21}|^2$ for the conductive PLA-filled MPRWG thru section are shown in Fig. 11(a) for both X- and Ku-bands. As expected, the blue lines show the insertion loss being consistently higher for propagation of the TE_{10} mode against layers; clearly demonstrating the anisotropic nature of FDM 3-D printed samples, even when printing with a theoretical 100% infill [30].

Depending on the length of MPRWG thru line, the dominant Fabry-Pérot (and TE_{101}, TE_{201}, TE_{011} and TE_{111} open-box mode) resonance frequencies may be found below the recommended lower waveguide band-edge frequency, because of the relatively high dielectric constant of conductive PLA; while higher-order modes may be found in-band. Moreover, because of the very high loss tangent, all modes will be heavily damped; causing extreme frequency broadening of all resonances. For this reason, distinct magnitude-frequency resonance features will not be easily seen in-band. Moreover, the influence from out-of-band Fabry-Pérot resonances may extend into and across the waveguide band. Fortunately, the phase-frequency response for the forward voltage-wave transmission coefficient $\angle S_{21}(f)$ is well-defined, even with very lossy dielectrics, and so this can be used to find (anti-)resonances. With TE_{m0} modes, it has been previously shown that the first-order Fabry-Pérot driven resonance frequency $f_{FP1} = f_{\lambda g/2}/\sqrt{\varepsilon'_{reff}}$ for a lossless dielectric [30]; the equality turns into an ever-greater approximation as the dielectric loss increases and as f_{FP1} moves ever-further below the recommended lower waveguide band-edge frequency. Similarly, with TE_{m0} modes, it can be shown that the first-order Fabry-Pérot driven anti-resonance frequency $f_{FPA1} = f_{\lambda g/4}/\sqrt{\varepsilon'_{reff}}$ for a lossless dielectric. Indeed, all orders of Fabry-Pérot (anti-)resonance frequencies can be determined by setting $l = p \cdot \lambda_g/4$, where $p \in [1, 2, 3, \ldots]$; odd-p gives $[N = (p+1)/2]$-order anti-resonances and even-p gives $[N = p/2]$-order resonances, where N is the order of destructive/constructive interference. Note that, with constructive transmission interference only, odd-N has even and even-N has odd electric $E_y(z)$-field symmetry, respectively, when looking at electromagnetic field simulations. Using the textbook expression for real guided-wavelength, with TE_{m0} modes, the Fabry-Pérot (anti-)resonance frequencies $f_{FP(A)}(p)$ for a lossless dielectric can be determined with the following closed-form analytical expression

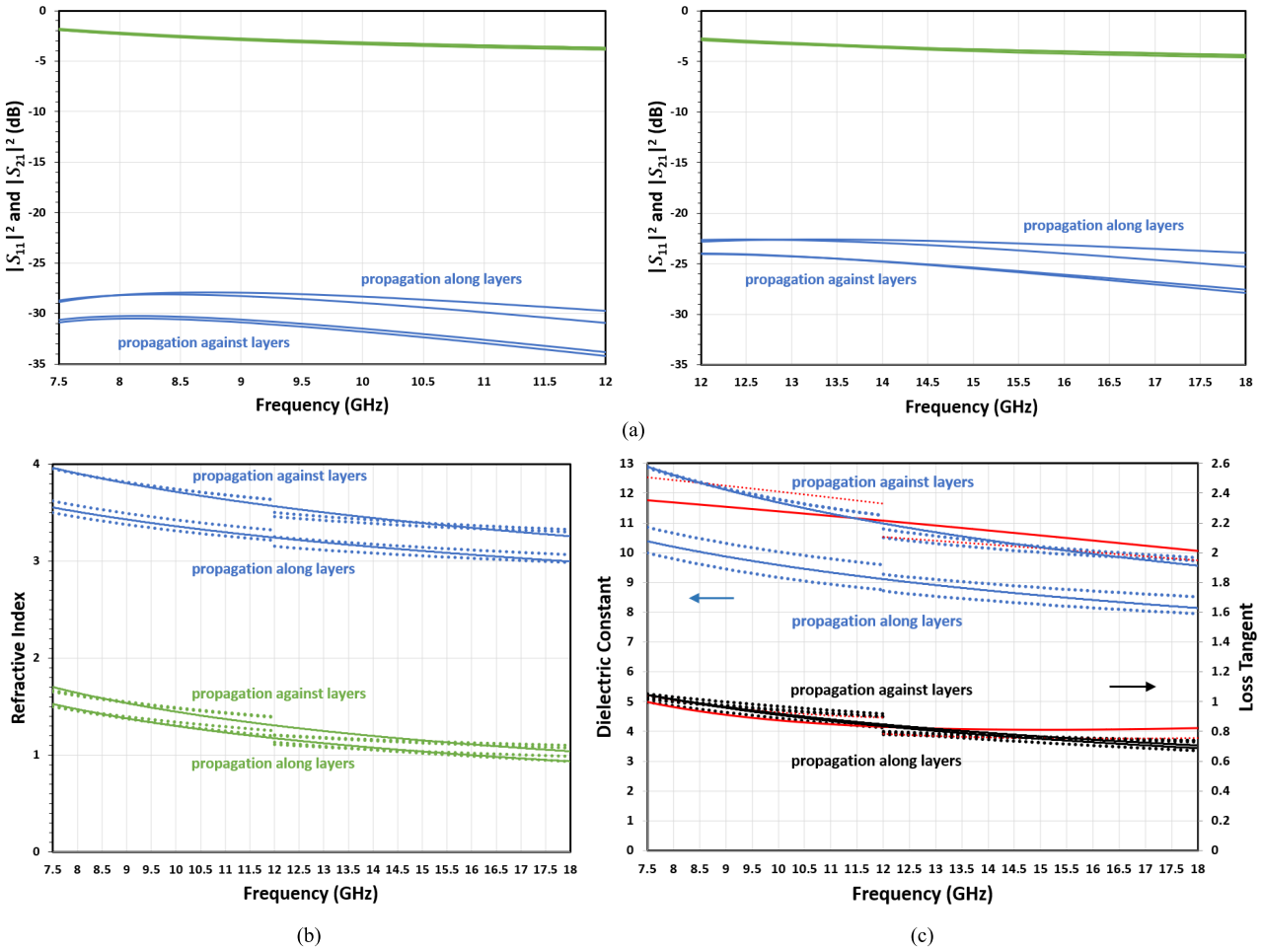

FIGURE 11. FDM 3-D printed Proto-pasta conductive PLA sample characterization at X- and Ku-bands: (a) loss measurements for the dielectric-filled MPRWG thru line, with $|S_{11}|^2$ in green and $|S_{21}|^2$ in blue (the latter has an typical uncertainty at NPL of ± 0.03 dB in these bands); (b) extracted complex refractive index $\tilde{n}$, with index of refraction n in blue and extinction coefficient κ in green; and (c) extracted complex effective relative permittivity $\tilde{\varepsilon}_{reff}$, with dielectric constant (Dk) ε'_{reff} in blue and loss tangent (Df) $tan\delta$ in black. Individual measurement extracted dielectric parameters are represented by dotted lines, while curve-fittings across combined X- and Ku-bands are represented by solid lines. Results from Pelton *et al.* dispersion modeling are represented by red dotted (individual bands) and solid (combined band) lines.

(for non-magnetic materials):

$$f_{FP(A)}(p) = \frac{c/\sqrt{\varepsilon'_{reff}}}{4l} \cdot \sqrt{p^2 + \left(\frac{2ml}{a}\right)^2} \tag{1}$$

However, for materials with arbitrary dielectric losses, the Fabry-Pérot (anti-)resonance frequencies cannot be determined using (1). Instead, the forward voltage-wave transmission coefficient S_{21} can be exploited using the following general expressions (for non-magnetic materials) [30]:

$$S_{21} = \left[\frac{1 - \Gamma_0^2}{1 - (\Gamma_0 P)^2}\right] P \tag{2}$$

where, the zero-order electric-field wave (or complex Fresnel) reflection coefficient Γ_0 at the interface between the reference air-filled and dielectric-filled sections of a MPRWG is,

$$\Gamma_0 = \frac{Z_{TEm0} - Z^{air}_{TEm0}}{Z_{TEm0} + Z^{air}_{TEm0}} \tag{3}$$

where, for TE_{m0} modes, the complex wave impedance Z_{TEm0} for a dielectric-filled MPRWG is,

$$Z_{TEm0} = \frac{\eta_o}{\sqrt{\tilde{\varepsilon}_{reff} - \left(\frac{m\lambda_o}{2a}\right)^2}} \tag{4}$$

and, for TE_{m0} modes, the complex wave impedance Z_{TEm0} for an air-filled MPRWG is,

$$Z^{air}_{TEm0} = \frac{\eta_o}{\sqrt{1 - \left(\frac{m\lambda_o}{2a}\right)^2}} \tag{5}$$

TABLE 2. In-band Fabry-Pérot (anti-)resonance frequencies extracted from the measured phase-frequency response for the forward voltage-wave transmission coefficient with TE_{10} mode propagation against layers.

Waveguide Band	Ideal Waveguide TE_{10} mode Cut-off Frequency (GHz)	Recommended Band-edge Frequencies		Ideal Waveguide TE_{20} mode Cut-off Frequency (GHz)	l (mm)	Quarter-wavelength Air-filled Waveguide Frequency, $f_{\lambda g/4}$ (GHz)	Half-wavelength Air-filled Waveguide Frequency, $f_{\lambda g/2}$ (GHz)	Fabry-Pérot (Anti-)Resonance Frequencies (GHz) Samples #1 / #2	
		Lower (GHz)	Upper (GHz)					f_{FP2}	f_{FPA3}
X-band (WR-90)	6.557	8.20	12.40	13.114	9.626	10.179	16.896	8.527/ 8.596	10.928/ 11.015
Ku-band (WR-62)	9.488	12.40	18.00	18.976	6.676	14.699	24.375	13.723/ 13.797	17.363/ 17.420

The complex propagation factor $P = e^{-j2\pi l/\tilde{\lambda}_g}$, where the complex guided-wavelength is,

$$\tilde{\lambda}_g = \frac{\lambda_o}{\sqrt{\tilde{\varepsilon}_{reff} - \left(\frac{m\lambda_o}{2a}\right)^2}} \tag{6}$$

where, η_o is the intrinsic impedance of free space and $\lambda_o = c/f$ is the wavelength in free space.

Now, using (2)-(6), we determine the Fabry-Pérot (anti-)resonance frequencies by solving for the following unwrapped/wrapped phase angle crossing points:

$$\angle S_{21}(f_{FP(A)})\big|_{unwrapped} \equiv -p \cdot \pi/2 \text{ for all (anti}-\text{) resonances} \tag{7}$$

$$\angle S_{21}(f_{FP(A)})\big|_{wrapped} \begin{cases} -\pi/2 & \text{odd anti} - \text{resonances} \\ \pm\pi & \text{odd resonances} \\ +\pi/2 & \text{even anti} - \text{resonances} \\ 0 & \text{even resonances} \end{cases} \tag{8}$$

It has been found, through differential-phase group delay simulations, that the in-band phase-frequency response of $\angle S_{21}(f)$ is almost linear when both $\varepsilon'_{reff} \gtrsim 17$ and $tan\delta \gtrsim 0.7$. As dielectric constant decreases below ~17, the minimum loss tangent must increase above ~0.7, to maintain linearity (e.g., when $\varepsilon'_{reff} \gtrsim 7$, $tan\delta \gtrsim 1$). Having (near-)linearity is useful, as it allows nearby out-of-band Fabry-Pérot (anti-)resonance frequencies to be predicted using linear extrapolation from in-band measurements.

For both X- and Ku-band, Table 2 shows the in-band Fabry-Pérot (anti-)resonance frequencies extracted from measurements for TE_{10} mode propagation against layers. With our choice of MPRWG thru line, only $f_{FP2}(p = 4)$ found from the $\angle S_{21}(f_{FP2}) = 0$ crossing point and $f_{FPA3}(p = 5)$ found from the $\angle S_{21}(f_{FPA3}) = -\pi/2$ crossing point are located in-band. Here, the worst-case discrepancies are only ±0.4% and ±0.25% in (anti-)resonance frequencies with similar sample pairs for X-band and Ku-band, respectively.

The original Nicolson-Ross-Weir (NRW) method (with wrapped phase angle correction) represents a well-established approach for extracting $\tilde{\varepsilon}_{reff}$ directly at microwave frequencies, with the use of a modern VNA [30]. However, this 'Original NRW' method suffers from a mathematical instability around the Fabry-Pérot resonance frequency and so this is not recommended [30]; this approach was used by Kjelgard *et al.* [32] and Kjelgard [33]. Fortunately, the 'Modified NRW' approach for extracting the combined complex value for $\tilde{\mu}_r\tilde{\varepsilon}_{reff}$ can be employed [30], since the complex effective relative permeability $\tilde{\mu}_r \cong 1$ (with both carbon and PLA being non-magnetic materials). Alternatively, $\tilde{\varepsilon}_{reff}$ can be extracted directly using both the manual graphical and automated renormalization spectroscopic approaches [30].

Note that the 'Modified NRW' method was not applied to the ABS characterization process. The reason is that the NRW methods inherently assume a lossless MPRWG thru line. Since the loss tangent of our ABS samples are so small, any MPRWG wall losses artificially inflate the extracted loss tangent of the cuboid; while this inflation is insignificant when compared to the loss tangent of conductive PLA.

Using the 'Modified NRW' approach (and confirmed using our automated renormalization spectroscopic method), the extracted dielectric properties for the conductive PLA samples are shown in Fig. 11(b) for complex refractive index $\tilde{n} = n - j\kappa = \sqrt{\tilde{\mu}_r\tilde{\varepsilon}_{reff}}$ and in Fig. 11(c) for the dielectric constant and loss tangent; again, treating both X- and Ku-bands independently. Here, all the extracted dielectric parameters for the individual cuboids are represented by dotted lines.

As expected, anisotropic behaviour can be clearly seen, with consistently higher values of complex refractive index and effective relative permittivity with propagation against layers. It is also found that, with propagation against layers, the similar sample pairs for each band gives consistent results, but those between bands differ; suggesting that linear spatial dimensional scaling laws may not apply to 'woodpile' type structures. With propagation along layers, none of the four cuboids give consistent results; suggesting that this print orientation is more sensitive to manufacturing tolerances. The extracted results from similar sample pairs were averaged (at each frequency) and purely empirical model curve fitting (using a simple power law) was applied across the combined X- and Ku-bands, represented by the solid lines in Figs. 11(b) and 11(c). The model parameters (with coefficient of determination $R^2 > 0.91$), as well as the more accurate fits for individual bands (with $R^2 > 0.99$), are given in Table 3. Resulting dielectric property values from

TABLE 3. Measurement extracted power law curve fitting parameters for dielectric constant (Dk) and loss tangent (Df).

			$\psi \cdot (f[GHz])^{\xi}$		
Propagation Direction	**Band**	**Dielectric Property**	**Scaling Constant ψ**	**Power Exponent ξ**	**Coefficient of Determination R^2**
Along Layers	**X**	**Dk**	18.168	-0.278	0.9919
		Df	2.0470	-0.344	0.9999
	Ku	**Dk**	15.298	-0.215	0.9990
		Df	1.6793	-0.301	0.9996
	X + Ku	**Dk**	18.168	-0.278	0.9919
		Df	2.7418	-0.479	0.9640
Against Layers	**X**	**Dk**	22.657	-0.283	0.9980
		Df	1.7541	-0.270	0.9998
	Ku	**Dk**	17.713	-0.206	0.9949
		Df	1.1855	-0.166	0.9984
	X + Ku	**Dk**	25.593	-0.340	0.9701
		Df	2.5786	-0.448	0.9136

the combined X- and Ku-band power law model are given in Table 1. From 9 to 10 GHz, against layers, the average dielectric constant and loss tangent are 11.9 and 0.89, respectively. Both values are approximately double those reported by Huber *et al.*, for the same frequency range, having respective values of 6.811 and 0.493 with their second method [24].

It has been shown here that FDM 3-D printed Protopasta conductive PLA is frequency dispersive across both X- and Ku-bands. However, the first-order approximation $\varepsilon''_{reff}(\omega) \sim (\omega\varepsilon_o\rho_o)^{-1}$, which exploits electrostatic measurements of intrinsic volume resistivity at DC, is oversimplistic. As a result, a physical model was used to characterize the cuboids over an extended frequency range. Here, the Pelton *et al.* dispersion model (similar in form to the Cole-Cole dispersion model) is applied to the complex effective volume resistivity (also known as 'impedivity' or 'specific impedance') $\rho(\omega) = \rho'(\omega) + j\rho''(\omega) = \left(j\omega\varepsilon_o\varepsilon_{reff}(\omega)\right)^{-1}$, where $\varepsilon''_{reff}(\omega) \neq \left(\omega\varepsilon_o\rho'(\omega)\right)^{-1}$ and $\rho''(\omega) < 0$ with a capacitive sample (normally associated with dielectric materials) [40]:

$$\rho(\omega) = \rho_\infty + \frac{\Delta\rho}{1 + (j\omega\tau)^{1-\alpha_\rho}} \tag{9}$$

where, ρ_o and ρ_∞ are the low frequency (DC) and high frequency (infinite) limits, respectively, of impedivity; $\Delta\rho = (\rho_o - \rho_\infty)$ is the impedivity increment; τ is a phenomenological relaxation time with $\omega_T = 1/\tau$ giving the 'top' angular frequency; $(1 - \alpha_\rho)$ is the Cole-Cole model exponent and $0 \leq \alpha_\rho \leq 1$ is the dispersion parameter [40]. Impedivity modeling is only applied to the more consistent similar sample pairs (having propagation against layers), for both X- and Ku-bands, as shown by the dotted red lines in Figs. 11(c) and 12.

It can be seen that the Pelton *et al.* dispersion model [40] can give a good fit to each individual band, using (9) with the parameter values given in Table 4. By taking the arithmetic mean parameter values from the individual bands, a crude combined band approximation can be made, as shown by the solid red lines in Figs. 11(c) and 12.

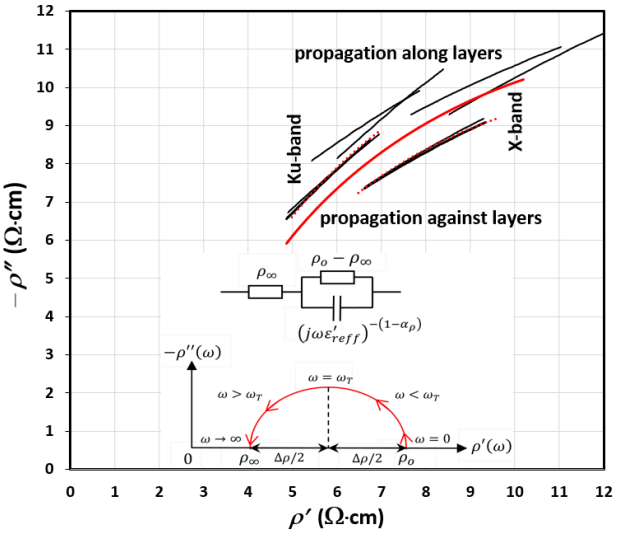

FIGURE 12. Complex impedivity plane mapping. Solid black lines represent extracted values for individual samples. Results from Pelton *et al.* dispersion modeling are represented by red dotted (individual bands) and solid (combined band) lines.

TABLE 4. Measurement extracted impedivity modeling parameter values with (9) for similar sample pairs having propagation against layers. Parameters for the combined band are the arithmetic means from the individual bands.

Band	**Measured Specific Density (g/cm^3)**	**Extracted Parameter**			
		ρ_o (Ω·cm)	**ρ_∞ (Ω·cm)**	**τ (ps)**	**α_ρ**
X	1.15	23.750	3.10	203.0	0.025
Ku	1.18	28.000	2.80	200.0	0.025
X + Ku	–	25.875	2.95	201.5	0.025

Impedivity modeling using (9) gives an indirect way of extrapolating the effective volume resistivity at DC. From Table 4, it can be seen that ρ_o is approximately one quarter of

the 115 Ω.cm value for measurement against layers reported by ProtoPlant [25], [26]. When comparing the parameter values for the individual X- and Ku-bands, it can be seen from Table 4 that there are ±5% and ±8% discrepancies between the high and low frequency limits of impedivity, respectively. The reason for this is unknown; the ±1.3% discrepancy in the measured specific density of the samples for the two bands does not fully account for this anomaly, with further investigation beyond the scope of this paper.

The very low frequency characteristics of any material represent an important datum point for frequency dispersion modeling. An initial attempt was made to directly characterize the effective volume resistivity at DC, with all our eight samples on display in Fig. 8(c), using four-point resistance measurements at DC. Our measurement holder was similar to that described by ProtoPlant. To minimize errors due to surface roughness, a very thin layer of aluminum foil makes conformal contact over the irregular flat surface of the 3-D printed cuboid. A copper wire mesh is pressed against the foil on one side, with a rigid insulating sponge on its other side. Finally, these two conformal electrode assemblies are attached to opposite faces of the cuboid with a G-clamp. It was interesting to observe the measured resistance exhibiting an inverse proportionality to both time and the force exerted by the G-clamp, irrespective of print orientation. In contrast to solid (non-3-D printed) dielectric cuboids, which could be measured satisfactorily, no stable measurements could be extracted from a resistance that continued to decrease with both time and force; while excessive G-clamp force also risked non-visible internal damage to the samples. In summary, our initial attempts to measure the DC resistance of the unique FDM 3-D printed conductive PLA cuboid samples (having a 'woodpile' type of structure) only produced unreliable (i.e., non-reproducible) results. This unusual behaviour deserves further investigation, which is beyond the scope of this paper. In addition, microwave measurements in other frequency bands would help to develop our Pelton *et al.* dispersion model; again, this is beyond the scope of this paper.

V. WAVEGUIDE TRANSITION RESULTS

Mated-pair transitions, illustrated in Fig. 4, were simulated using the commercial electromagnetic High Frequency Structure Simulator (HFSS) software. Here, the extracted dielectric properties for conductive PLA, given in Table 3, were used. The resulting S-parameter predictions, along with the associated measurements are given in Fig. 13. It can be seen that our PolyJet 3-D printed mated-pair back-to-back transitions generally has a measured insertion loss between 0.6 and 0.8 dB and input return loss better than 20 dB, across Ku-band; both matching well with predictions.

There are also unpredicted ripples in the measured results, being most pronounced between 15 and 16 GHz; this may be attributed to the damped excitation of the TE_{21} mode. Nevertheless, the overall measured performance across Ku-band pays testament to the excellent combination of employing PolyJet 3-D printing and commercial Jet Metal^{TM} silver spray metalization.

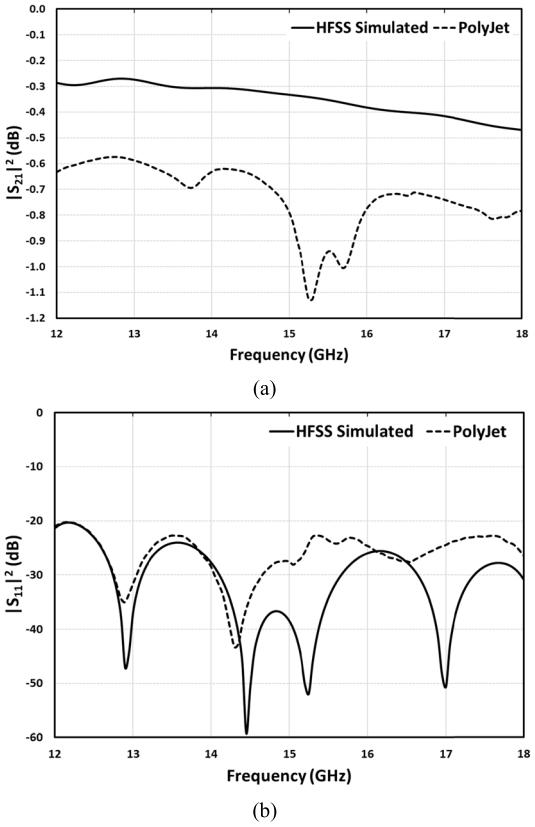

FIGURE 13. Measured PolyJet performance and associated HFSS simulated predictions for the mated-pair back-to-back transitions illustrated in Fig. 4: (a) $|S_{21}|^2$ responses; and (b) $|S_{11}|^2$ responses.

VI. ROTARY VANE ATTENUATOR RESULTS

Figure 14(a) shows the experimental setup for the assembled rotary vane attenuator, while Fig. 14(b) shows the various resistive vanes slotted *in situ* into one transition and the rotating central section having an average internal radius of 10.35 mm (being approximately 2.3% larger than the ideal value).

As with the mated-pair transitions, HFSS simulations were performed using the extracted dielectric properties for conductive PLA, given in Table 3. The predicted performance is shown in Figs. 15(a) and 15(b) for the transmission and reflection responses, respectively. The insertion loss response is relatively flat across Ku-band, having a mid-band attenuation range of 20 dB; while the input return loss is better than 20 dB, from 13 to 18 GHz, across the 78° tuning range. Moreover, changes in attenuation increase with incremental increases in the value of rotational angular offset, due to the sec(θ) dependency; resulting in the expected increase in tuning sensitivity as $\theta \rightarrow 90°$. As expected, Fig. 15(c) shows that the predicted monotonic behaviour of the differential-phase group delay response does not vary significantly across Ku-band over the 78° tuning range.

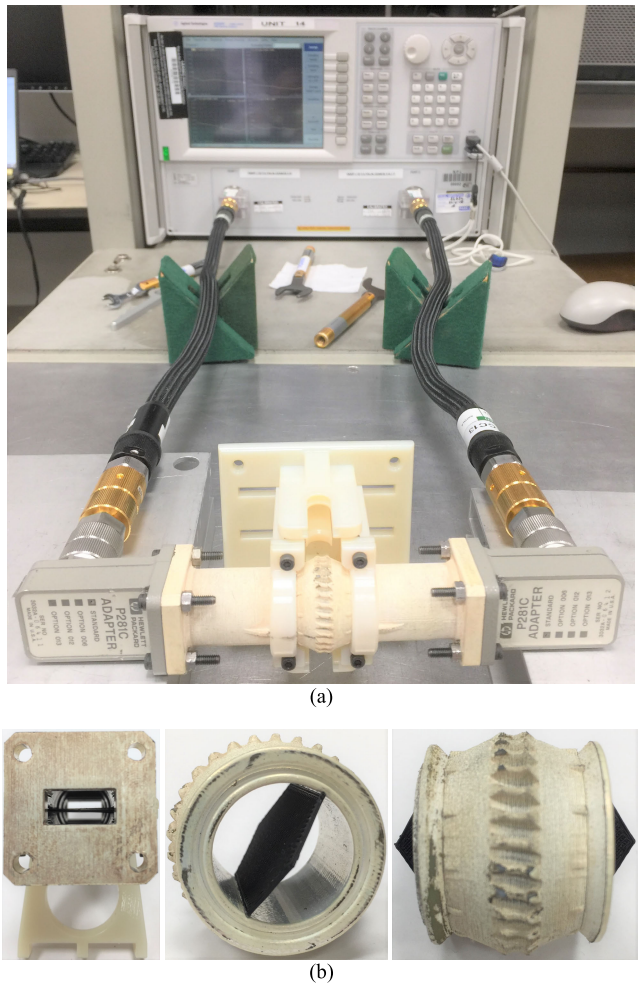

FIGURE 14. Photographs of the all 3-D printed rotary vane attenuator: (a) complete assembly being measured *in situ*; (b) waveguide port view of mode-matching transition (left), internal view of rotating center section (middle) and side view of rotating center section (right). The black quasi-planar septa are the FDM 3D-printed Proto-pasta conductive PLA resistive vanes.

Figure 16 shows the measured performance of our 3-D printed RVA, which closely matches the predicted simulated performance given in Fig. 15. For example, the measured levels of insertion loss are almost identical for $\theta \in [0, 6, 18, 30, 42, 54]$, with higher attenuation levels beyond this range of rotational angular offset – due to the increasing tuning sensitivity to our basic 3-D printed tuning screw implementation. Nevertheless, with $\theta = 78°$, the mid-band tuning range has increased to 29 dB.

The theoretical and measured tuning behavior for the 3-D printed prototype RVA is given Fig. 17, at mid-band and both band edges. In practice, the ideal theoretical model should also include losses, in the form of a maximum insertion loss, represented by an additional attenuation off A_{off} term [3]:

$$A\,(\text{dB}) = 10log_{10}\left\{\sec^4(\theta)\right\} + A_{off}\,(\text{dB}) \qquad (10)$$

where $A_{off} \sim 1.2$ dB is extracted from a good visual fit in Fig. 17. Of particular note is that the measured results

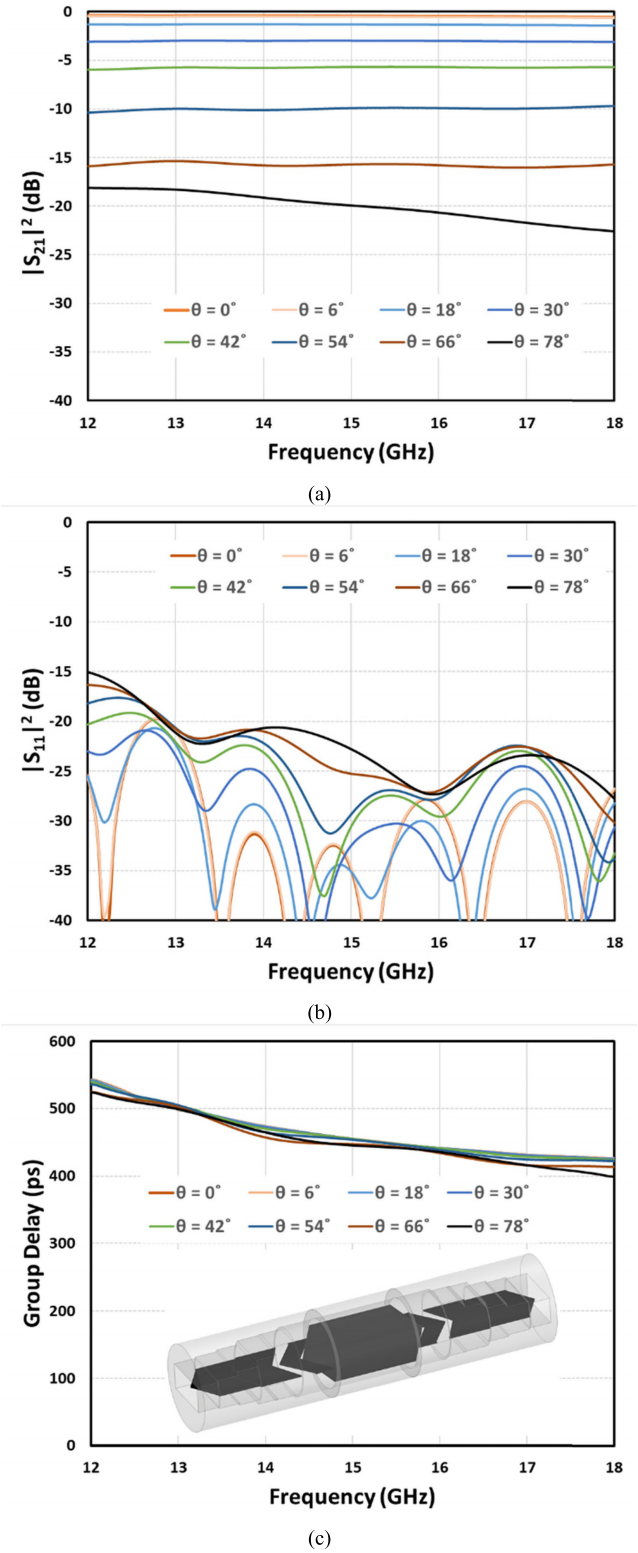

FIGURE 15. HFSS predicted RVA S-parameters for different values of angular rotational offset θ: (a) $|S_{21}|^2$ responses; (b) $|S_{11}|^2$ responses; and (c) differential-phase group delay with HFSS model insert.

closely match the theoretical law for all values of rotational angular offset. However, this cannot be said for the HFSS simulation results with $\theta \gtrsim 66°$; possibly due to the excitation

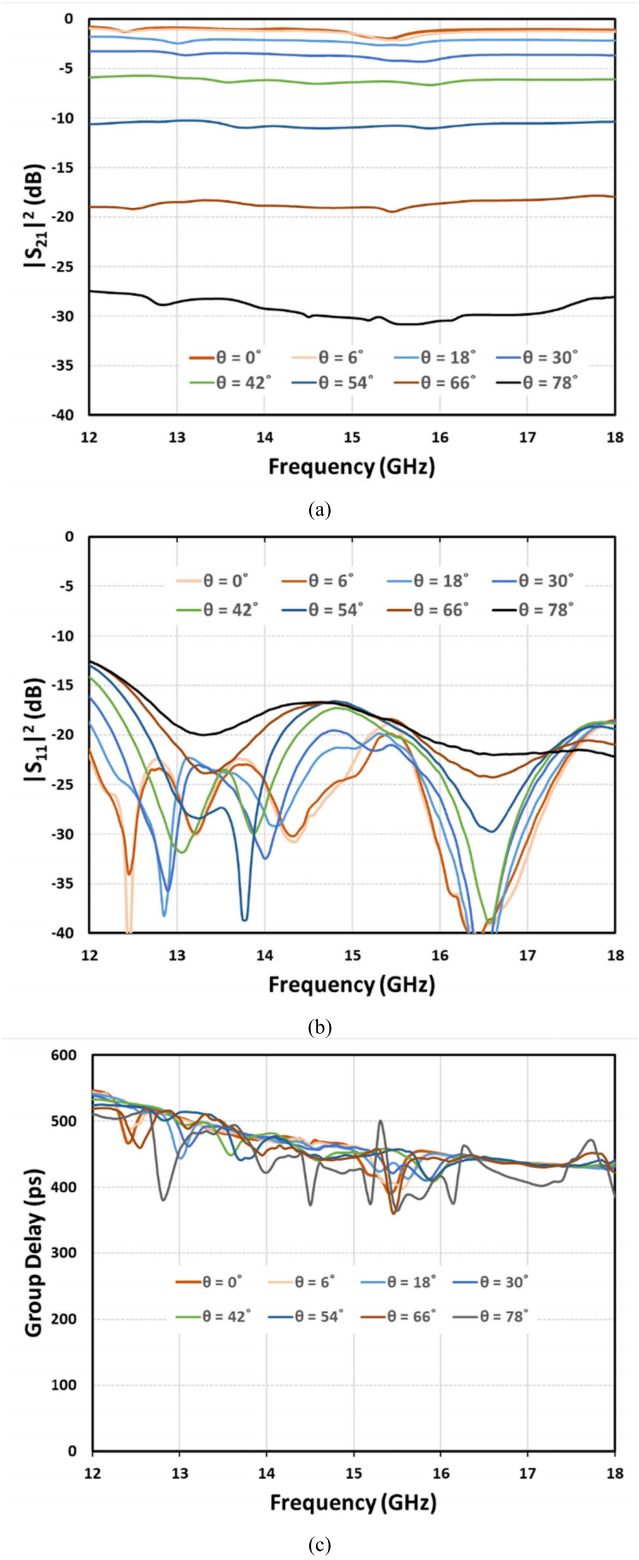

FIGURE 16. Measured RVA S-parameters for different values of angular rotational offset θ: (a) $|S_{21}|^2$ responses; (b) $|S_{11}|^2$ responses; and (c) differential-phase group delay.

of an unwanted mode, caused by issues associated with inadequate meshing [30].

The measured input return loss is 17 dB, from 12.7 to 18 GHz, across our 78° tuning range. Finally, the measured differential-phase group delay is reasonably well behaved.

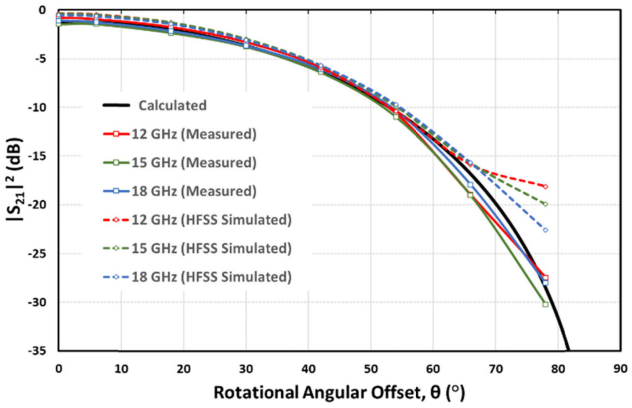

FIGURE 17. Calculated and measured RVA tuning behaviors at mid-band and band edges.

TABLE 5. Ku-band RVA performance comparison with our 3-D printed prototype against commercial specifications for a conventional machined counterpart (Flann Precision RVA, model 18110 [41]).

Performance Parameter	This Work (3-D Printed)	Commercial (Machined)
Attenuation Range (dB)	0-27	0-60
Maximum Insertion Loss (dB)	1.2	0.3
Worst-Case Return Loss (dB)	17 (12.7 to 18 GHz)	23
Mass (kg)	0.050	3.4

Table 5 gives a performance comparison with our non-optimized 3-D printed prototype RVA against a top-of-the-range commercial counterpart that employs traditional machining technology [41]. It can be seen that while our RVA does not meet the extremely high levels of performance set by the precision instrument, our 3-D printed technology is much smaller, lighter (having only 1.5% of the mass) and cheaper to manufacture.

VII. CONCLUSION

This paper demonstrates the potential of rapid prototyping for the manufacture of ultra-light weight microwave rotary vane attenuators using polymer-based 3-D printing. Without any prior expertise in manufacturing RVAs, the authors previously presented the preliminary results for the prototype design [9]. This early work has now been greatly expanded here; giving detailed design information and presenting the superior measurement results using re-worked resistive vanes.

In addition, for the first time, conductive PLA has been rigorously characterized from 8 to 18 GHz; while ABS has similarly been characterized from 12 to 18 GHz. Using the results from the conductive PLA characterization process, an electromagnetic model was created for predicting the performance of the RVA.

It has been shown that, even with its complex internal geometrical features, a mix of both dielectric and conductive PLA building materials, an assembly of multiple parts and a mechanically rotating central section, our experimental proof-of-concept prototype RVA exhibits excellent measured performance across Ku-band. While not matching the microwave performance of a top-of-the-range commercial counterpart, our 3-D printed RVA has less than 1.5% of its mass.

This tunable microwave control device represents a higher-level of functionality for additive manufacturing, when compared to a fixed (i.e., non-movable) 3-D printed structure. With ever-continuing advancements in commercial 3-D printer technologies and their building materials, the performance of microwave components and subsystems manufactured using additive manufacturing will continue to improve. Moreover, as the costs associated with 3-D printing decrease with time, it may be commonplace for research and development groups to routinely 3-D print custom microwave components and subsystems in the not too distant future.

We believe that this 3-D printed RVA can be used as a general purpose wideband attenuator and so it is likely to be used in many radar, communications and measurement systems that would normally employ either a fixed value or variable attenuator.

ACKNOWLEDGMENT

The authors would like to thank M. Mirzaee and S. Noghanian, previously at the University of North Dakota (USA), and also K. G. Kjelgård, from the University of Oslo (Norway), for giving additional details of their conductive PLA research. They also appreciate the help of J. Skinner at NPL for undertaking the VNA measurements.

REFERENCES

[1] W. Larson, *The Rotary-Vane Attenuator as an Interlaboratory Standard*, vol. 144. Gaithersburg, MD, USA: National Bureau of Standards Monograph, 1975.
[2] A. V. James, "A high-accuracy microwave-attenuation standard for use in primary calibration laboratories," *IRE Trans. Instrum.*, vols. 1–11, no. 3/4, pp. 285–290, Dec. 1962.
[3] T. Guldbrandsen, "Precision model for microwave rotary vane attenuator," *IEEE Trans. Instrum. Meas.*, vol. IM-28, no. 1, pp. 59–66, Mar. 1979.
[4] P. A. Rizzi, *Microwave Engineering: Passive Circuits*. Upper Saddle River, NJ, USA: Prentice-Hall, 1988, pp. 324–326.
[5] R. E. Collin, *Foundations for Microwave Engineering*, 2nd ed. Hoboken, NJ, USA: Wiley, 2001, pp. 397–400.
[6] M. D'Auria, W. J. Otter, J. Hazell, B. T. W. Gillatt, C. Long-Collins, N. M. Ridler, and S. Lucyszyn, "3-D printed metal-pipe rectangular waveguides," *IEEE Trans. Compon., Packag., Manuf. Technol.*, vol. 5, no. 9, pp. 1339–1349, Sep. 2015.
[7] B. T. W. Gillatt, M. D'Auria, W. J. Otter, N. M. Ridler, and S. Lucyszyn, "3-D printed variable phase shifter," *IEEE Microw. Wireless Compon. Lett.*, vol. 26, no. 10, pp. 822–824, Oct. 2016.
[8] S.-H. Shin, D. F. Alyasiri, M. D'Auria, W. J. Otter, C. W. Myant, D. Stokes, Z. Tian, N. M. Ridler, and S. Lucyszyn, "Polymer-based 3-D printed Ku-band steerable phased-array antenna subsystem," *IEEE Access*, vol. 7, pp. 106662–106673, Aug. 2019.
[9] E. Márquez-Segura, W. J. Otter, S. Lucyszyn, and N. Ridler, "Fabricación aditiva de atenuadores variables de veleta rotatoria en guía de onda," in *Proc. XXXIV Nat. Symp. Int. Radio Sci. Union (URSI)*, Seville, Spain, Sep. 2019, pp. 1–4.
[10] A. Jones, S. Lucyszyn, E. Márquez-Segura, N. Ridler, J. Skinner, and D. Stokes, "3-D printed standards for calibration of microwave network analysers," *Measurement*, vol. 158, pp. 1–10, Jul. 2020.
[11] W. J. Otter and S. Lucyszyn, "Hybrid 3-D-printing technology for tunable THz applications," *Proc. IEEE*, vol. 105, no. 4, pp. 756–767, Apr. 2017.
[12] W. J. Otter, N. M. Ridler, H. Yasukochi, K. Soeda, K. Konishi, J. Yumoto, M. Kuwata-Gonokami, and S. Lucyszyn, "3D printed 1.1 THz waveguides," *Electron. Lett.*, vol. 53, no. 7, pp. 471–473, Mar. 2017.
[13] S.-H. Shin, X. Shang, N. M. Ridler, and S. Lucyszyn, "Polymer-based 3-D printed 140–220 GHz low-cost quasi-optical components and integrated subsystem assembly," *IEEE Access*, vol. 9, pp. 28020–28038, Feb. 2021.
[14] K. Y. Chan, R. Ramer, and R. Sorrentino, "Low-cost Ku-band waveguide devices using 3-D printing and liquid metal filling," *IEEE Trans. Microw. Theory Techn.*, vol. 66, no. 9, pp. 3993–4001, Sep. 2018.
[15] W. Larson, "Analysis of rotation errors of a waveguide rotary-vane attenuator," *IEEE Trans. Instrum. Meas.*, vol. IM-12, no. 2, pp. 50–55, Sep. 1963.
[16] T. Y. Otoshi and C. T. Stelzried, "A precision compact rotary vane attenuator," *IEEE Trans. Microw. Theory Techn.*, vol. MTT-19, no. 11, pp. 843–854, Nov. 1971.
[17] S. Stuchly and A. Kraszewski, "Wide-band rectangular to circular waveguide mode and impedance transformer (correspondence)," *IEEE Trans. Microw. Theory Techn.*, vol. MTT-13, no. 3, pp. 379–380, May 1965.
[18] M. A. Morgan and S.-K. Pan, "Graphical prediction of trapped mode resonances in sub-mm and THz waveguide networks," *IEEE Trans. THz Sci. Technol.*, vol. 3, no. 1, pp. 72–80, Jan. 2013.
[19] L. Solymar, "Spurious mode generation in nonuniform waveguide," *IRE Trans. Microw. Theory Techn.*, vol. 7, no. 3, pp. 379–383, Jul. 1959.
[20] R. Walker, "Analysis and correction of echo due to mode conversion in WC-281 waveguide," *IEEE Trans. Microw. Theory Techn.*, vol. 43, no. 3, pp. 592–600, Mar. 1995.
[21] Stratasys. *CONNEX3 OBJECT260*. Accessed: Mar. 29, 2021. [Online]. Available: https://www.stratasys.com/3d-printers/objet260-connex3
[22] Stratasys. *Digital ABS Plus*. Accessed: Mar. 29, 2021. [Online]. Available: https://www.stratasys.com/materials/search/digital-abs-plus
[23] A. Jammes, E. D. Gayets, K. Staelens, R. Feger, T. Lampersberger, and A. Stelzer, "Silver metallization of 77 GHz 3D printed horn antennas," in *Proc. 12th Eur. Conf. Antennas Propag. (EuCAP)*, London, U.K., 2018, pp. 1–4.
[24] E. Huber, M. Mirzaee, J. Bjorgaard, M. Hoyack, S. Noghanian, and I. Chang, "Dielectric property measurement of PLA," in *Proc. IEEE Int. Conf. Electro Inf. Technol. (EIT)*, Grand Forks, ND, USA, May 2016, pp. 788–792.
[25] (Mar. 28, 2015). *Electrically Conductive PLA 3D Printer Filament*. Accessed: Mar. 29, 2021. [Online]. Available: https://www.kickstarter.com/projects/1375236253/electrically-conductive-pla-3d-printer-filament
[26] *Electrically Conductive Composite PLA*. Accessed: Mar. 29, 2021. [Online]. Available: https://www.proto-pasta.com/products/conductive-pla
[27] P. F. Flowers, C. Reyes, S. Ye, M. J. Kim, and B. J. Wiley, "3D printing electronic components and circuits with conductive thermoplastic filament," *Additive Manuf.*, vol. 18, pp. 156–163, Dec. 2017.
[28] M. Mirzaee and S. Noghanian, private communication, Jan. 2021.
[29] (Dec. 2017). *Keysight 85070E Dielectric Probe Kit 200 MHz to 50 GHz: Technical Overview*. Accessed: Mar. 29, 2021. [Online]. Available: https://www.keysight.com/gb/en/assets/7018-01196/technical-overviews/5989-0222.pdf
[30] J. Sun, A. Dawood, W. J. Otter, N. M. Ridler, and S. Lucyszyn, "Microwave characterization of low-loss FDM 3-D printed ABS with dielectric-filled metal-pipe rectangular waveguide spectroscopy," *IEEE Access*, vol. 7, pp. 95455–95486, Jul. 2019.
[31] B. Faenger, S. Ley, M. Helbig, J. Sachs, and I. Hilger, "Breast phantom with a conductive skin layer and conductive 3D-printed anatomical structures for microwave imaging," in *Proc. 11th Eur. Conf. Antennas Propag. (EUCAP)*, Paris, France, Mar. 2017, pp. 1065–1068.
[32] K. G. Kjelgard, D. T. Wisland, and T. S. Lande, "3D printed wideband microwave absorbers using composite graphite/PLA filament," in *Proc. 48th Eur. Microw. Conf. (EuMC)*, Madrid, Spain, Sep. 2018, pp. 859–862.
[33] G. Kjelgard, private communication, Dec. 2020.
[34] *Keysight N1500A Materials Measurement Software Suite: Technical Overview*. Accessed: Mar. 29, 2021. [Online]. Available: https://www.keysight.com/us/en/assets/7018-04630/technical-overviews/5992-0263.pdf

[35] A. I. Hernandez-Serrano, Q. Sun, E. G. Bishop, E. R. Griffiths, C. P. Purssell, S. J. Leigh, J. Lloyd-Hughes, and E. Pickwell-MacPherson, "Design and fabrication of 3-D printed conductive polymer structures for THz polarization control," *Opt. Exp.*, vol. 27, no. 8, pp. 11635–11641, Apr. 2019.
[36] J. Sun and S. Lucyszyn, "Extracting complex dielectric properties from reflection-transmission mode spectroscopy," *IEEE Access*, vol. 6, pp. 8302–8321, Mar. 2018.
[37] Cura. (2019). *Ultimaker*. Accessed: Mar. 29, 2021. [Online]. Available: https://ultimaker.com/software/ultimaker-cura
[38] IdeaMaker. (2019). *Raise3D*. Accessed: Mar. 29, 2021. [Online]. Available: https://www.raise3d.com/ideamaker/
[39] F. Castles, D. Isakov, A. Lui, Q. Lei, C. E. J. Dancer, Y. Wang, J. M. Janurudin, S. C. Speller, C. R. M. Grovenor, and P. S. Grant, "Microwave dielectric characterisation of 3D-printed $BaTiO_3$/ABS polymer composites," *Sci. Rep.*, vol. 6, no. 1, pp. 1–8, Mar. 2016.
[40] A. Tarasov and K. Titov, "On the use of the Cole–Cole equations in spectral induced polarization," *Geophys. J. Int.*, vol. 195, pp. 352–356, Jul. 2013.
[41] Flann Microwaves. *Precision Rotary Vane Attenuators*. Accessed: Mar. 29, 2021. [Online]. Available: https://flann.com/products/attenuators/precision-rotary-vane-attenuators/

ENRIQUE MÁRQUEZ-SEGURA (Senior Member, IEEE) was born in Málaga, Spain, in April 1970. He received the Ingeniero de Telecomunicación and Doctor Ingeniero degrees from the Universidad de Málaga, Málaga, in 1993 and 1998, respectively.

In 1994, he joined the Departamento de Ingeniería de Comunicaciones, Escuela Técnica Superior de Ingeniería (ETSI) de Telecomunicación, Universidad de Málaga, where he became an Associate Professor, in 2001. His research interests include electromagnetic material characterization, additive manufacturing, measurement techniques, RF, microwave, and millimeter-wave circuits design for communication applications. He was a recipient of the Spanish Ministry of Education and Science Scholarship, from 1994 to 1995.

SANG-HEE SHIN (Graduate Student Member, IEEE) was born in Seoul, South Korea, in 1992. He received the M.Eng. degree in aeronautical engineering from Imperial College London, London, U.K., in 2018, where he is currently pursuing the Ph.D. degree within the Department of Electrical and Electronic Engineering.

His research interests include designing and manufacturing RF and quasi-optical systems for microwave and mm-wave applications using additive manufacturing techniques.

ATTIQUE DAWOOD received the M.S. degree in electrical engineering from the National University of Computer and Emerging Sciences, Islamabad, Pakistan, in 2012, and the Ph.D. degree from Imperial College London, London, U.K., in 2020. His current research interest includes electromagnetic modeling of passive structures from microwaves to terahertz frequencies.

NICK M. RIDLER (Fellow, IEEE) received the B.Sc. degree in physics from King's College London, University of London, London, U.K., in 1981.

He is currently the Head of Science within the Department of Electromagnetic and Electrochemical Technologies, National Physical Laboratory, Teddington, U.K. He is an NPL Fellow and a Visiting Professor with the University of Leeds, U.K., the University of Liverpool, U.K., and the University of Surrey, U.K., and a Nonexecutive Director of LA Techniques, Ltd. He is a fellow of the Institution of Engineering and Technology (IET) and the Institute of Physics (IOP). He has about 40 years of experience working in industrial, government, and academic research establishments. His main research interest includes precision high-frequency electromagnetic measurement (from 1 kHz to 1 THz).

STEPAN LUCYSZYN (Fellow, IEEE) received the Ph.D. degree in electronic engineering from King's College London, University of London, London, U.K., in 1992, and the D.Sc. degree (Hons.) in millimetre-wave and terahertz electronics from Imperial College London, London, in 2010.

He is currently a Professor of millimetre-wave systems with Imperial College London. He has coauthored well over 200 articles and 12 book chapters in applied physics and electronic engineering. He was made a fellow of the Institution of Electrical Engineers, U.K., and the Institute of Physics, U.K., in 2005. In 2008, he became a fellow of the Electromagnetics Academy, USA. He was appointed as an IEEE Distinguished Microwave Lecturer, from 2010 to 2013. He co-founded the Imperial College London spin-out company Drayson Wireless Ltd., in 2014.